



Cite this: DOI: 10.1039/d5cc02438b

# Five key concepts linking vacancies, structure, and oxygen evolution reaction activity in cobalt-based electrocatalysts

Kenneth Crossley, <sup>a</sup> Thomas J. Schmidt <sup>ab</sup> and Emiliana Fabbri <sup>\*a</sup>

Received 30th April 2025,  
Accepted 10th July 2025

DOI: 10.1039/d5cc02438b

rsc.li/chemcomm

Green hydrogen, produced *via* water electrolysis, is a promising next-generation energy vector. The oxygen evolution reaction (OER) is the rate limiting half-reaction for water electrolysis. OER electrocatalyst cost and performance are important factors impeding global water electrolysis scale up. In an acidic environment, typical industrial OER electrocatalysts are

precious metal-based materials (IrO<sub>x</sub>, RuO<sub>x</sub>). In an alkaline environment, less expensive and more abundant transition metal (hydr)oxides based on Fe, Co, and Ni are becoming competitive. Herein we focus on Co-based electrocatalysts, but the conclusions should generally be applicable to other Fe- and Ni-based materials.

The prevailing aspiration to increase the activity of Co-based (hydr)oxides is to selectively switch the OER mechanism. The prototypical adsorbate evolution mechanism (AEM)—exhibiting concerted proton/electron transfer—has a fundamental activity

<sup>a</sup> PSI Center for Energy and Environmental Science, 5232 Villigen PSI, Switzerland.

E-mail: emiliana.fabbri@psi.ch

<sup>b</sup> Institute for Molecular Physical Science, ETH Zürich, CH-8093 Zürich, Switzerland


Kenneth Crossley

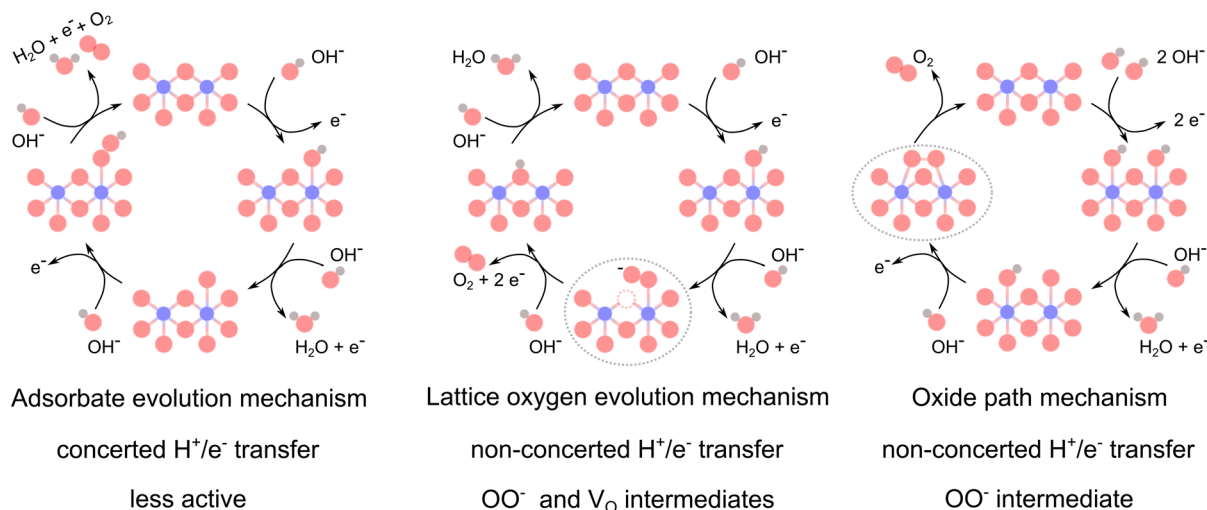
*Kenneth Crossley previously studied physics (BA, Colorado College) and materials science/chemistry through the SERP+ Erasmus Mundus program (MS, University of Genoa/Université Paris-Saclay). He is currently a doctoral candidate at ETH Zürich focused on next generation oxygen evolution reaction electrocatalysts in the Electrocatalysis and Interfaces group at the Paul Scherrer Institute (PSI). Outside the lab he enjoys fly fishing, rock climbing, drawing, skiing, and cycling.*



Thomas J. Schmidt

*Prof. Thomas J. Schmidt is a Professor and Chair for Electrochemistry, ETH Zürich and Head of the PSI Center for Energy & Environmental Research at PSI. He is also the Director of the Swiss Center of Excellence on Netzero Emissions. He graduated with a PhD in chemistry at the University of Ulm, Germany and then continued his career as a postdoc and a scientist at Lawrence Berkeley National Laboratory and at PSI. He spent eight years in industrial fuel cell research (BASF Fuel Cell) as Director of R&D. Between 2014 and 2021, he also acted a Director of the Swiss Competence Center for Energy Research (SCCER) Heat & Electricity Storage. His work is focused on all aspects of electrochemical energy conversion and storage.*





**Scheme 1** Proposed mechanisms for the alkaline OER. Co atoms are shown in blue, O in red, H in grey, and oxygen vacancies ( $\text{V}_\text{O}$ ) in dashed red circles. The characteristic steps with superoxide  $\text{OO}^-$  intermediates are indicated with grey dashed ellipses. Scheme inspired by Rong *et al.*<sup>14</sup>

limit imposed by universal adsorption energy scaling relationships.<sup>1</sup> Conversely, the lattice oxygen evolution reaction (LOER) breaks these activity limitations *via* non-concerted proton/electron transfer and involves an O–O coupling step between the surface lattice oxygen and adsorbed oxygen species.<sup>2,3</sup> It is suggested that LOER activation requires a covalent M–O electronic structure with O 2p character near the Fermi level.<sup>4</sup> The LOER cannot be activated without accompanying dissolution and surface reconstruction under applied potential,<sup>5,6</sup> but a dynamic equilibrium can be established to balance activity and durability.<sup>7–9</sup>

Multiple LOER mechanisms (LOEMs) have been proposed—including intramolecular nucleophilic attack,<sup>10</sup> Mars van Krevelen,<sup>11</sup> and lattice oxygen mechanism (LOM)<sup>4,12,13</sup>—all of which dynamically create/fill oxygen vacancies ( $\text{V}_\text{O}$  in the

Kröger–Vink notation). The oxide path mechanism (OPM) has also been proposed to occur *via* O–O radical coupling between adjacent metal adsorbate sites when the metal–metal distance is short enough, although it is more common in acidic conditions.<sup>14</sup> The AEM, LOEM, and OPM are depicted in Scheme 1. Presently, it remains difficult to experimentally differentiate between, and selectively activate, these non-AEM mechanisms (see Concept 3).

In this review, we highlight recent works which indicate key variables to control surface reconstruction pathways, active site geometry, and selective mechanism activation. We structure these works around five key concepts with a view towards fundamental/mechanistic OER understanding.

## 1 Vacancies do more than dangle bonds

Recent works on amorphous OER catalysts/amorphous surface layers often attribute increased activity to flexible structure, increased surface area, or dangling bonds.<sup>15–17</sup> While these geometric factors certainly contribute, the effects of oxygen vacancies are far more nuanced, can be disentangled far more rigorously, and do not universally improve catalytic activity.

The primary effects of oxygen vacancies are modulating the adsorption site density and free energies of adsorption. As clearly investigated and summarized by Tao *et al.*, introducing surface oxygen vacancies to p-type semiconductors shifts the hybridized O 2p–M 3d antibonding states closer to the Fermi level and increases the metal site adsorption energy of O intermediates on pristine precatalysts.<sup>18</sup> Note that density functional theory (DFT) calculations of adsorption energies on the actual reconstructed active surfaces remain elusive. Moreover, high bulk oxygen vacancy concentrations can down-shift the O 2p band and reduce the catalytic activity.<sup>19</sup>



**Emiliana Fabbri**

*particularly interested in the surface chemistry and electronic structure of catalysts studied by operando X-ray synchrotron techniques. Emiliana Fabbri was awarded an SNSF PRIMA grant in 2020 and since 2024 she is co-leader of the Electrocatalysis and Interfaces group of the Electrochemistry Laboratory of PSI.*

*Dr Emiliana Fabbri received her PhD in Materials Science from the University of Rome Tor Vergata. In 2009 she was appointed tenured scientist at the National Institute for Materials Science (NIMS), Japan. Since January 2012, she has been working at PSI in Switzerland on materials for electrochemical energy storage and conversion. To gain a fundamental understanding of electrochemical reaction mechanisms and catalytic activity descriptors, she is*



Particularly in double perovskites such as  $\text{PrBaCo}_2\text{O}_{6-\delta}$ , high oxygen deficiency ( $\delta \approx 0.5$ ) can lead to bulk ordering of oxygen vacancies, decreasing conductivity, and a detrimental  $\text{Co}^{3+}$  high-to-low spin state transition.<sup>20</sup> Cheng *et al.* examined a  $\text{La}_{1-x}\text{Sr}_x\text{CoO}_{3-\delta}$  series, a  $\text{LaMO}_{3-\delta}$  series ( $\text{M} = \text{Cr}, \text{Mn}, \text{Fe}, \text{Co}, \text{Ni}$ ),  $\text{Ba}_{0.5}\text{Sr}_{0.5}\text{Co}_{0.8}\text{Fe}_{0.2}\text{O}_{3-\delta}$  and  $\text{PrBaCo}_2\text{O}_{6-\delta}$  perovskites and found  $\delta > 0.2$  to be desirable for OER applications.<sup>21</sup>

Intuitively, the  $\text{OH}^-$  and  $\text{H}_2\text{O}$  species can also adsorb to oxygen vacancies. Oxygen vacancies and  $\text{OH}^-$  adsorption have been linked to initiating surface reconstruction in many Co-based electrocatalysts including  $\text{CoSn}(\text{OH})_6$ ,<sup>22</sup>  $\text{CoMoO}_4/\text{CoWO}_4/\text{Co}_2\text{VO}_4$ ,<sup>23</sup>  $\text{Co}(\text{OH})_2$ ,<sup>24</sup> and  $\text{Co}_3\text{O}_4$ .<sup>25</sup> The roles of these adsorption sites and species in surface reconstruction are examined in more depth in Concept 4.

Cation vacancies can also positively affect the OER activity. Chen *et al.* used Ar plasma treatment on  $\text{Co}_{0.9}\text{Fe}_{0.1}\text{Sn}(\text{OH})_{6-\delta}$  to selectively form Sn and O vacancies.<sup>26</sup> The cation vacancy selectivity was achieved by a relative difference in M–OH bond strengths between the cations. Their defective material showed increased hydrophilicity, a Co/Fe-rich amorphous surface layer, and enhanced electrochemical activity compared to the untreated parent material. Their DFT results suggest that the selective Sn–O vacancies decreased the coordination number and free energy of O adsorption ( $\Delta G^0(\text{O}^*) = 3.69$  vs. 2.49 eV) at the Co sites, leading to a lower Tafel slope (77 vs. 42 mV  $\text{dec}^{-1}$ ) and a shift in the rate determining step compared to the pristine material. Zhang *et al.* have also demonstrated beneficial Co vacancies in  $\text{Co}_{3-x}\text{O}_4$  derived from glycerolcobalt(II) pyrolysis.<sup>27,28</sup> The Co vacancies were confirmed combining X-ray diffraction (XRD), transmission electron microscopy (TEM) energy dispersive spectroscopy, and positron annihilation lifetime spectroscopy measurements. Their DFT results suggest that the Co vacancies introduce a high density of unoccupied states above the Fermi level and increase electron delocalization. These combined effects yielded a turnover frequency an order of magnitude higher than that of pristine  $\text{Co}_3\text{O}_4$ .

The extent of dissolution-derived Co vacancies during alkaline OER depends on the precatalyst structure, the presence of other metal ions, the pH, and the applied potential. Moysiadou and Hu used *operando* electrochemical quartz crystal microbalance and inductively coupled plasma optical emission spectroscopy (ICP-OES) to determine the dissolution rates of amorphous electrodeposited  $\text{CoO}_x$ ,  $\text{CoFeO}_x$ , and  $\text{CoFeNiO}_x$  in 1 M KOH at 1.58 V vs. RHE (reversible hydrogen electrode).<sup>29</sup> The  $\text{CoFeNiO}_x$  mass remained constant, but  $\text{CoFeO}_x$  and  $\text{CoO}_x$  showed 20–30% mass loss in the first 6 h before equilibrating with trace Fe adsorption from the electrolyte. In contrast, crystalline  $\text{Co}_3\text{O}_4$  and  $\text{CoFe}_2\text{O}_4$  (111) epitaxial thin films remain stable except for sub-nanometer dissolution and reconstruction at the surface.<sup>30,31</sup> Lopez *et al.* coupled rotating disk electrode and inductively coupled plasma mass spectrometry (ICP-MS) characterizations to evaluate *operando* dissolution in  $\text{La}_{1-x}\text{Sr}_x\text{CoO}_3$  nanoparticles.<sup>32</sup>  $\text{La}_{1-x}\text{Sr}_x\text{CoO}_3$  showed increasing Co dissolution with increasing Sr content, but negligible Co dissolution above 1.5 V vs. RHE in pristine 0.1 M KOH and at all tested potentials when 1 ppm Fe was introduced into the electrolyte. Conversely,  $\text{CoOOH}$  on Pt showed an increasing rate of Co

dissolution in the Fe contaminated electrolyte above 1.4 V vs. RHE and a  $3\times$  lower stability factor. Mn incorporation has also been shown to help stabilize Co dissolution.<sup>33,34</sup> Overall, it is becoming clear that a dynamic equilibrium must be achieved between the catalyst bulk, reconstructed surface, and transition metal ions in the double layer (see Concept 4).<sup>7,8</sup>

Vacancies created by introducing sacrificial cations in the structure can also selectively influence the active site population, stability, and geometry. Menezes *et al.* demonstrated that selective Zn etching from  $\text{ZnCo}_2\text{O}_4$  preferentially exposes octahedral Co sites at the reconstructed interface.<sup>35</sup> Ca- and Fe-dominated dissolution in brownmillerite-type  $\text{Ca}_2\text{FeCoO}_5$  drives the transformation to an amorphous  $\text{CoOOH}$  structure which is stable for at least 4 weeks under OER conditions.<sup>36</sup> Wei *et al.* investigated a  $\text{La}_{0.3}\text{Sr}_{0.7}\text{Co}_{1-x}\text{Al}_x\text{O}_{3-\delta}$  material series and concluded that  $\text{Al}^{3+}$  dissolution initiated surface reconstruction *via* oxygen vacancy formation, but that the equilibrium state down-shifted the O 2p band and prevented continued bulk reconstruction.<sup>37</sup> Liu *et al.* found that this dynamic equilibrium of  $\text{Al}^{3+}$  dissolution/ $\text{Al}(\text{OH})_n^-$  adsorption was responsible for improved activity, stability, and  $\text{Cl}^-$  repulsion in  $\text{CoFeAl}$  layered double hydroxides (LDHs) exhibiting high sea water electrolysis performance.<sup>9</sup>

## 2 The effect of surface oxygen vacancies is facet-dependent

Using  $\text{NaBH}_4$  reduction of  $\text{Co}_3\text{O}_4$  nanoparticles, Chen *et al.* introduced surface oxygen vacancies to cubic ((001) facets) and truncated octahedron ((111) majority, (001) minority facets) geometries.<sup>38</sup> Both types of defective particles outperformed their pristine parent materials, yet, the defective cubic material showed an order of magnitude higher activity and  $2\text{--}4\times$  greater pH dependence than the pristine cubic and defective octahedral particles. Their DFT results indicate that the upshift of the O 2p band center for the (001) facet reduced the Co 3d and O 2p interband center gap and increased the overlapping O and Co density of unoccupied states just above the Fermi level. There was little change for the (111) facet. Along with *operando* Raman spectroscopy and tetramethylammonium (TMA) oxygen radical quenching measurements, these findings point to the selective activation of the LOEM on oxygen deficient  $\text{Co}_3\text{O}_4$  (001). This AEM to LOEM shift and the relation to surface reconstruction is further discussed in Concepts 3 and 4. Davis *et al.*<sup>39</sup> and Wei *et al.*<sup>40</sup> have shown that the extent of  $\text{Co}_3\text{O}_4$  surface reconstruction is also facet-dependent.

Considering other  $\text{Co}_3\text{O}_4$  facets, Shojaei *et al.*'s DFT calculations reveal that it is easier to form oxygen vacancies on the  $\text{Co}_3\text{O}_4$  (100) facet than the (110) facet.<sup>41</sup> Similarly, the  $\text{Co}_3\text{O}_4$  (220) facet has been calculated to have an even lower oxygen vacancy formation energy,<sup>42</sup> which could be advantageous to exploit for OER.

This facet dependence is not limited to  $\text{Co}_3\text{O}_4$ .  $\text{Co}(\text{OH})_2$  derived  $\beta\text{-CoOOH}$  hexagonal nanosheets have been shown to preferentially drive OER on the lateral facets, with the larger area (0001) basal planes being mainly inactive.<sup>43,44</sup> Similar





lateral facet-dominant activity and facet-dependent reconstruction has also been confirmed for NiOOH nanosheet OER catalysts.<sup>45</sup> Introducing oxygen vacancies to the lateral (10 $\bar{1}$ 0) facets slightly reduces the rate determining potential barrier ( $-0.05$  V), whereas a reduction of  $-0.4$  V is seen for the (0001) and (1 $\bar{1}$ 00) facets.<sup>44</sup> This large barrier reduction indicates that a combined doping/dissolution plus oxygen vacancies engineering strategy may be sufficient to activate the CoOOH/NiOOH basal (0001) plane for OER.

### 3 The OER mechanism can be controlled *via* oxygen vacancy concentrations

Differentiating between the multiple OER mechanisms remains a challenge. The LOEM and OPM show pH-dependent activity, the order of which should be determined with a fixed overpotential to avoid mixed kinetic-thermodynamic reaction order changes. The intermediate  $O_2^-$  radical is present in both the LOEM and OPM, which can be detected *via* TMA quenching,<sup>12,38</sup> the  $^{18}O/^{16}O$  kinetic isotope effect,<sup>46</sup> or Fourier transform infrared spectroscopy.<sup>38,47,48</sup> Labeling catalysts with  $^{18}O$  isotopes along with online mass spectrometry<sup>10,19,49</sup> or *operando* Raman spectroscopy<sup>50</sup> can help differentiate between the AEM, LOEM, and OPM. *Operando* application of one or more of these techniques aids in the mechanistic interpretation of pH-dependent activity.

To decouple the multiple effects of introducing oxygen vacancies by aliovalent cation doping, Lu *et al.* employed ball milling for incremented times to increase the oxygen vacancy concentrations in a series of  $La_xSr_{1-x}CoO_{3-\delta}$  (LSCO- $\delta$ ) materials with fixed cation stoichiometries.<sup>19</sup> The activity change of this doping + ball milled oxygen vacancies series is reproduced in Fig. 1. The authors clearly demonstrate that increasing the oxygen deficiency can either deactivate the LOEM (high Sr content, Fig. 1(A)) or activate the LOEM/LOM (high La content, Fig. 1(B) and (C)) during CV cycling depending on the Co 3d and O 2p band alignments. In the case of deactivation, the activity-limiting “lockup effect” reflects decreasing participation of the possible OER active sites as the material’s cation reducibility

limit is approached with increasing oxygen deficiency.<sup>6,19</sup> Beyond pH-dependent activity and DFT calculations, their Raman spectroscopy results also demonstrate switchable surface reconstruction pathways associated with CoOOH formation.

LOER activation does not appear to be dependent on the method of oxygen vacancy introduction. When Chen *et al.* introduced surface oxygen vacancies to their cubic  $Co_3O_4$  nanoparticles *via*  $NaBH_4$  reduction, they detected increased OER activity and pH dependence compared to the pristine material which followed the AEM.<sup>38</sup> Their *operando* Raman measurements showed peaks at 1095 and 1125  $cm^{-1}$ , which correspond to Co–O–O–Co vibrational modes and indicate an  $O_2^-$  intermediate formed by a LOEM or OPM. In addition, the activity decreased with TMA– $O_2^-$  quenching. These results indicate the selective activation of an  $O_2^-$  radical-producing mechanism on  $Co_3O_4$  (001) facets. Similarly, Zhou *et al.* created surface oxygen vacancies in  $Co_3O_4$  *via* chemical reduction with increasing concentrations of  $NaBH_4$ .<sup>10</sup> Their electrochemical, kinetic isotope effect, *operando* Raman spectroscopy, and online mass spectrometry characterizations indicate that the oxygen vacancies activated the LOER and shifted the mechanism to intramolecular nucleophilic attack (metal-adsorbed O attacking adjacent lattice O). However, as discussed in Concept 4, high oxygen vacancy densities can also introduce quenching mechanisms that limit the OER activity.

### 4 Vacancies can steer the surface reconstruction pathway and ultimate catalyst activity

Universally, metal (hydr)oxide catalysts have thermodynamically unstable interfaces under OER conditions and will self-reconstruct with varying degrees of dissolution.<sup>5</sup> Fabbri *et al.* first applied *operando* X-ray absorption spectroscopy (XAS) to observe the surface reconstruction of oxygen deficient  $Ba_{0.5}Sr_{0.5}Co_{0.8}Fe_{0.2}O_{3-\delta}$  to form a  $(CoFe)O_x(OH)_y$  layer.<sup>7</sup> Using *operando* and *ex situ* freeze-quenched XAS, Bergmann *et al.* demonstrated that CoO (in rock salt and wurtzite structure),  $Co_3O_4$ , and CoOOH all reconstruct to a principally octahedrally-

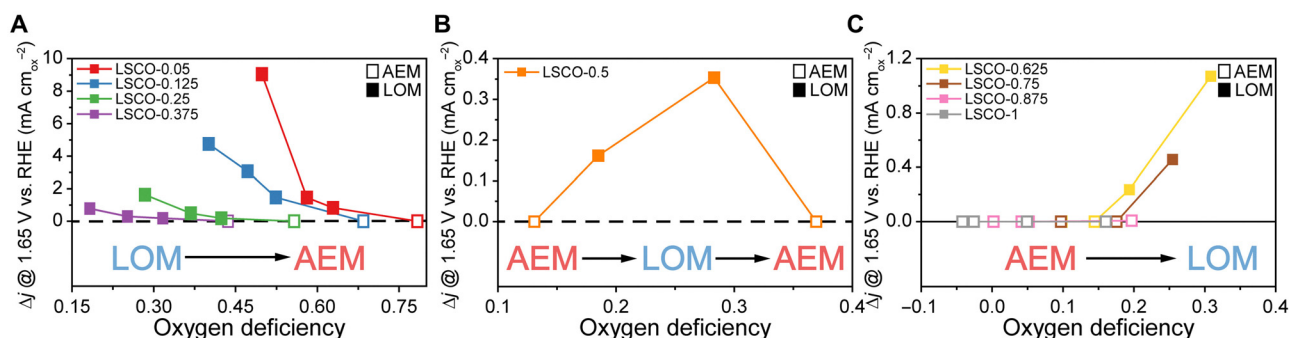


**Fig. 1** Patterns in OER mechanism shifts for  $La_xSr_{1-x}CoO_{3-\delta}$  (LSCO- $\delta$ ). (A) Increasing oxygen deficiency in the high Sr regime deactivates the LOEM. (B) Increasing oxygen deficiency in the mid Sr/La regime activates and then deactivates the LOEM. (C) Increasing oxygen deficiency in the La majority regime activates the LOEM, but the high La range always follows the AEM.  $\Delta j$  is the normalized current density difference from the initial to the maximum activity cycle. For each material, moving left to right increments the ball milling time (0, 2, 4, 6 h). Reproduced from Lu *et al.* (CC-BY-NC 4.0).<sup>19</sup>



coordinated 3D cross-linked  $\text{CoO}_x(\text{OH})_y$  surface layer under neutral and alkaline OER conditions.<sup>51</sup> They identified reducible di- $\mu$ -oxo-bridged  $\text{Co}^{3+}$  ions as the reconstructed active site common to all these materials. Despite a common meta-stable active layer, a wide range of activities are observed for Co-based OER electrocatalysts. The reconstruction pathway is key to determining the final activity.

There is mounting evidence that Co (hydr)oxide surfaces with oxygen vacancies take different reconstruction pathways compared with their pristine counterparts. Using *operando* XAS and X-ray photoelectron spectroscopy (XPS), Xiao *et al.* demonstrated that Ar plasma-derived oxygen vacancies increase the adsorption of OH groups at lower potentials compared to defect-free  $\text{Co}_3\text{O}_4$ .<sup>25</sup> Their defective  $\text{Co}_3\text{O}_4$  displayed a lower charge transfer resistance above 1.15 V vs. RHE and a faster rate of oxidation/deprotonation before 1.45 V vs. RHE. Moreover, Alex *et al.* have shown that crystalline  $\text{Co}_3\text{O}_4$  with oxygen vacancies can have higher reconstructed intrinsic activity and outperform nanocrystalline/amorphous  $\text{Co}_3\text{O}_4$ .<sup>52</sup> Despite minimal long range order and  $4.7\times$  more surface area, the nanocrystalline catalyst was reported to have fewer surface oxygen vacancies (based on the troublesome O 1s XPS adsorbed OH peak, see Concept 5) and a lagging Tafel slope of 153 mV dec<sup>-1</sup>. Conversely, Liu *et al.* reported that amorphous  $\text{Co}(\text{OH})_2$  nanocages with abundant oxygen vacancies (detected by electron paramagnetic resonance) outperform crystalline  $\text{Co}_3\text{O}_4$  and demonstrate faster oxidation/reduction at lower potentials.<sup>24</sup> Overall, it is becoming clear that (oxy)hydroxide species adsorbed on or near oxygen vacancies can reconstruct more easily than on fully ordered facets.

Xiao *et al.* insightfully utilized *operando* Raman spectroscopy to observe the surface reconstruction of pristine and oxygen deficient  $\text{CoMoO}_4$ ,  $\text{CoWO}_4$ , and  $\text{Co}_2\text{VO}_4$ .<sup>23</sup> They showed that oxygen vacancies accelerate Mo/W/V dissolution, thus exposing more oxygen vacancies and Co sites. Oxygen vacancy-adsorbed OH and  $\text{H}_2\text{O}$  then formed hydrated amorphous  $\text{Co}(\text{OH})_2$  within 5 min at 1.15 V vs. RHE. Within 5 min at 1.2 V vs. RHE, the intercalated amorphous  $\text{Co}(\text{OH})_2$  converted to  $\text{CoOOH}$ . Intriguingly, when the defective samples were soaked at open circuit potential in 1 M KOH for 60 min, the oxygen vacancies were filled, and  $\text{CoO}_x$  and crystalline  $\text{Co}(\text{OH})_2$  formed. Neither the pristine materials nor the 60 min soaked samples displayed the Raman shifts associated with either water adsorption or  $\text{CoOOH}$  formation at 1.2 V vs. RHE. Both had lower OER activities than the fresh defective sample. Such a defect adsorption/ $\text{H}_2\text{O}$  intercalation reconstruction mechanism at least partially explains why  $\text{CoOOH}$  reconstructed from boride/phosphide/sulfide precatalysts often outperforms directly synthesized  $\text{CoOOH}$  and  $\text{Co}_3\text{O}_4$ .<sup>53–58</sup> Taken together, these results suggest that  $\text{H}_2\text{O}$  adsorption and intercalation into the reconstructed  $\text{Co}(\text{OH})_2/\text{CoOOH}$  with an applied potential are necessary for high activity.

Akin to the  $\alpha/\beta\text{-Ni}(\text{OH})_2$  system, Leng *et al.*<sup>59</sup> and Sanchis-Gual *et al.*<sup>60</sup> examined  $\beta\text{-Co}(\text{OH})_2$ , and anion/ $\text{H}_2\text{O}$  intercalated  $\alpha\text{-Co}(\text{OH})_2$  as OER precatalysts. They found that  $\alpha\text{-Co}(\text{OH})_2$  exhibited the most reconstruction. Leng *et al.*<sup>59</sup> and Dionigi *et al.*<sup>61</sup> further confirmed that  $\beta/\alpha\text{-Co}(\text{OH})_2$  selectively

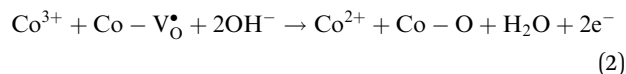
reconstruct to  $\beta/\gamma\text{-CoOOH}$ , with  $\gamma\text{-CoOOH}$  exhibiting the higher OER activity. Recently, Wang *et al.* stabilized  $\gamma\text{-CoOOH}$  in an alkaline electrolyzer and demonstrated 1 at 1.78 V.<sup>62</sup> These results further confirm that the reconstructed  $\text{CoOOH}$  layers OER activity depends on the reconstruction pathway.

K. Fan *et al.* have proposed different surface reconstruction pathways for  $\text{CoOOH}$ -like surfaces.<sup>63</sup> As shown in Scheme 2, after oxidation of  $\text{Co}^{2+}$  species to  $\beta\text{-CoOOH}$  species, a bifurcation occurs. A slow deprotonation and water intercalation step leads to  $\gamma\text{-CoOOH}_x$ , which can then be further oxidized to the OER active site or quenched by dense oxygen vacancy concentrations. A faster deprotonation pathway to  $\beta\text{-CoO}_2$  produces sites with lower intrinsic activity.<sup>63</sup> Based on the works previously discussed in this section, we propose an additional pathway mediated by oxygen vacancies and intercalated electrolyte species which proceeds directly to  $\gamma\text{-CoOOH}_x$  or a Co LDH structure.

In regions with high oxygen vacancy density, there is evidence suggesting an additional reconstruction pathway which quenches the oxidized Co active sites. For example, Zhou *et al.*'s highest oxygen vacancy concentration sample (1 M  $\text{NaBH}_4$  treatment) displayed two distinct electronic environments and a lower turnover frequency than the intermediate vacancy concentration sample.<sup>10</sup> Fan *et al.* proposed the following quenching reaction for high oxygen vacancy density environments which increases the number of reconstructed  $\text{Co}^{2+}$  spectator sites.<sup>63</sup>



We have included the  $\text{Co}^{4+}$  species by convention, but the quenched species could also be a  $\text{Co}^{3+}$  coordinated with a oxygen ligand electron hole in covalent systems. The authors proposed that amorphous materials are more prone to this quenching pathway, which may contribute to an increasing degree of crystallinity in amorphous catalysts during/post OER. However, such a chemical reaction does not explain the third anodic peak (A2 in Scheme 2) observed between the typical  $\text{Co}^{2+/3+}$  (A1) and  $\text{Co}^{3+/4+}$  (A3) peaks in some amorphous or high oxygen vacancy materials.<sup>10,24</sup> An additional electrochemical reaction which could account for this activity quenching in high oxygen vacancy density regions below the  $\text{Co}^{3+/4+}$  oxidation potential follows.

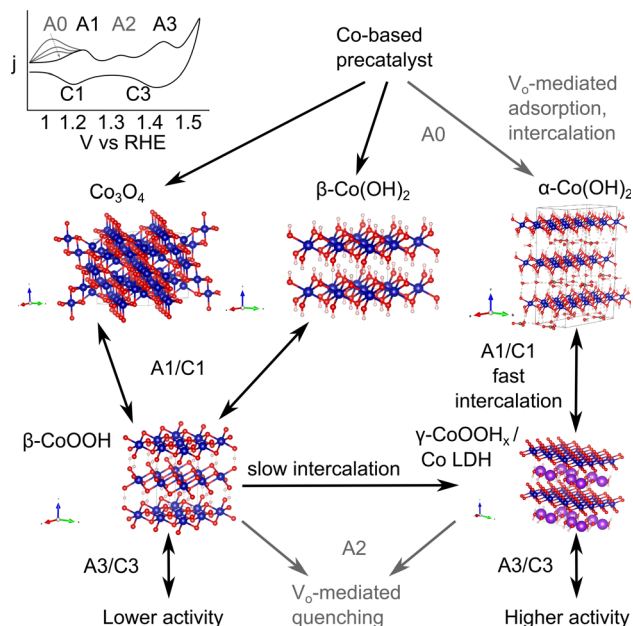


Regardless of the exact species/mechanism(s), note that such quenching reactions are dynamic competing processes during surface reconstruction, whereas the lockup effect originates from a fundamental charge conservation limit.

## 5 Oxygen vacancy quantification is complex and demands user knowledge

To determine exact oxygen vacancy thresholds to steer the reaction mechanism and surface reconstruction pathways, we need robust quantification strategies to be widely implemented. However, many of these techniques are misused or





**Scheme 2** The surface reconstruction pathways followed by Co-based OER catalysts. Oxygen is shown in red, hydrogen in cream, and cobalt in blue.  $\alpha$ -Co(OH)<sub>2</sub> is intercalated by water and anions (i.e. CO<sub>3</sub><sup>2-</sup> with C shown in brown), whereas  $\gamma$ -CoOOH<sub>x</sub> is intercalated by cations (i.e. K<sup>+</sup> shown in purple).<sup>61</sup> Co<sub>3</sub>O<sub>4</sub>,<sup>64</sup>  $\beta$ -Co(OH)<sub>2</sub>,<sup>65</sup>  $\beta$ -CoOOH<sub>x</sub>,<sup>66</sup> data accessed via the Crystallography Open Database. Note that the more active intermediate form of  $\gamma$ -CoOOH<sub>x</sub> vs. a Co layered double hydroxide (LDH) structure is not yet fully clear and may be material specific.

misunderstood in the interdisciplinary electrocatalysis literature. The advantages and disadvantages of various oxygen vacancy quantification techniques are summarized in Table 1.

### 5.1 Near surface techniques

The recent trend of using the fitting area ratio of XPS O 1s peaks at approximately 530 eV (lattice O) and 531–532 eV (often misattributed to oxygen vacancies) to quantify oxygen vacancy densities is fundamentally incorrect.<sup>67,68</sup> In the case of the O 1s region, XPS measures electrons ejected from core atomic orbitals; thus, there cannot be a signal from a chemical species defined by a missing O atom. Using *in situ* XPS, Yamamoto *et al.* have clearly demonstrated that the 531–532 eV features are characteristic of OH groups formed by the dissociation of water on metal or metal oxide surfaces.<sup>69</sup> This process will spontaneously fill surface oxygen vacancies upon contact with ambient water vapor or electrolyte.<sup>2,39,67</sup> Although there is a correlation with this surface hydroxyl spectral feature and surface reconstruction/subsequent OER activity,<sup>10,25</sup> using the hydroxyl XPS O 1s peak method is not a robust measure of oxygen vacancy concentrations because there are multiple surface hydroxyl adsorption sites<sup>70</sup> and spectral overlaps with contaminants (i.e. Na/K/Ca/Mg chlorides {Auger}, (bi)carbonates).<sup>70,71</sup>

Despite this recent trend, it is often possible to quantify surface oxygen vacancies in a more precise manner using XPS. Wang *et al.* advocate a three-fold quantification strategy using cation valence state peak ratios, lattice O 1s peak ratios, and

binding energy shifts.<sup>68</sup> For the cation valence state peak ratio approach, one must account for/exclude cation protonation and anion redox. When using the lattice O 1s peak approach, one must first normalize the spectra to the baseline or a redox-inactive cation peak intensity. Then the normalized lattice O peak ( $A(\approx 530 \text{ eV})$ ) fitting area can be compared to a fully oxidized surface using the following equation.<sup>68</sup>

$$\delta = 1 - \frac{A(\text{O}_{\text{lattice}})}{A(\text{O}_{\text{lattice}})_{\text{oxidized}}} \quad (3)$$

If sample charging, band bending, and space-charge layer effects are minimal, the binding energy shift can be a third strategy to quantify oxygen vacancy concentrations. One must understand the sample to select the appropriate method with XPS.

Alternatively, Li *et al.* have developed a rapid, inexpensive, and quantitative colorimetric method to detect surface oxygen vacancies in oxide catalysts.<sup>72,73</sup> As depicted in Fig. 2, this method uses the surface oxygen vacancy sites of the material to catalyze the decomposition of H<sub>2</sub>O<sub>2</sub> in a pH 4 buffer. The liberated hydroxides subsequently deprotonate the amine groups in the 3,3',5,5'-tetramethylbenzidine probe. This reaction changes the color from clear to turquoise and is quantified with an optical absorbance measurement. Although this method gives an indirect quantification of surface oxygen vacancies, it has the advantages of background subtraction and dynamically probing the vacancy sites accessible for OER in a liquid environment.

### 5.2 Bulk techniques

Electron paramagnetic resonance (EPR) is also frequently used for semi-quantitative oxygen vacancy characterization. Yet, only single unpaired electrons trapped at oxygen vacancies are directly detected at the common  $g \approx 2.002$  signal, which represents only a subset of the oxygen vacancy population.<sup>74</sup> A rigorous quantification requires analysis of the catalysts valence state (cation reduction) and magnetic structure.<sup>74–77</sup>

Given accurate cation ratio constraints, hard XAS allows bulk oxygen vacancies to be calculated. First, the cation K-shell absorption edge energy is detected. Then, standards of known oxidation state are used to linearly correlate edge energies with the oxidation state. Finally, the oxygen content is determined by charge neutrality of the cation oxidation state. Fitting neutron diffraction data can give more precise information on oxygen vacancies; however, large amounts ( $\approx 4 \text{ g}$ ) and highly crystalline samples are usually required.<sup>78</sup> XRD using a synchrotron source can be used for smaller masses, yet the technique is inherently less sensitive than neutron diffraction to light elements and their disorder.

Thermogravimetric analysis (TGA) can be used to directly measure the mass loss associated with the formation of oxygen vacancies; however, one should know the exact off-gassing species (H<sub>2</sub>O, CO<sub>2</sub>, O<sub>2</sub>) to make an accurate back calculation of the O content and origin. TGA coupled with in-line ICP-MS or ICP-OES can simultaneously detect the exhaust gas composition. Our experience suggests that a high purity sample is



**Table 1** Summary of the advantages and disadvantages of oxygen vacancy quantification methods. Accuracy in this context is a qualitative metric balancing precision (typical reproducible significant figures) and specificity (target species sensitivity, technique limitations)

Technique	Accuracy	Advantages	Disadvantages
XPS O 1s 531–532 eV	Low	None	Measures hydroxyls, not $V_O$
XPS cation oxidation + normalized lattice O 1s + binding energy	Medium	Quantitative treatment possible	Material specific choices/knowledge requirements
$H_2O_2$ /probe redox + colorimetric detection	Medium	Probes surface $V_O$ in a liquid environment	Requires standards, unproven hydroxide catalyst applicability
EPR spectroscopy	Medium	Directly detects single electrons trapped at $V_O$	Full quantification requires valence state/magnetic characterization
X-ray diffraction	Medium	Low sample masses possible	Less sensitive to light elements
Neutron diffraction	High	High sensitivity to light elements	Large masses, specialized facilities
X-ray absorption spectroscopy	Medium high	Sensitive to bulk $V_O$	Less sensitive to surface $V_O$
Thermogravimetry	Medium high	Directly measures mass loss for thermal/gaseous $V_O$ creation	Gas species detection (ICP-MS/OES) required for definitive attribution
Iodometric titration	Very high	Standard O quantification	Difficult back calculation for multiple, multi-valent transition metals

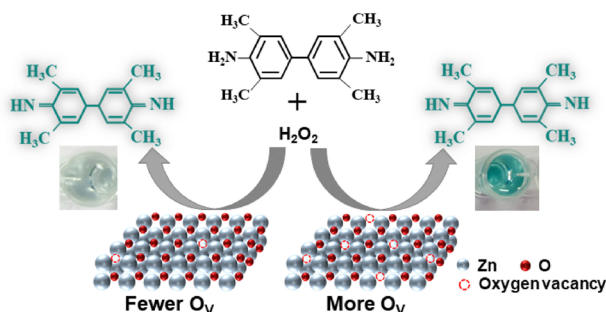


**Fig. 2** A schematic view of the colorimetric surface oxygen vacancy quantification method demonstrated by Li *et al.*<sup>72</sup> Reprinted with permission from Elsevier, copyright 2025.

required to avoid ambiguous signals from incorporated/adsorbed solvents and trace byproducts.

Iodometric titration can give precise oxygen stoichiometry results, but the sample should be a single phase and ideally contain only one metal ion with changing oxidation state for accurate back calculation.<sup>78,79</sup> A thorough understanding of the valence states of multimetallic oxides, especially Co and Fe, should be obtained with a complementary technique to avoid ambiguous titration results. Selective complexation can help isolate different ions in some cases.<sup>80</sup>

## 6 Summary and future perspectives

In Concept 1, we clarify that the effects of oxygen vacancies include shifting the electronic band alignments, adsorbing reaction intermediates, and initiating surface reconstruction. Cation vacancies can also affect the adsorption energies and surface reconstruction pathway *via* relative dissolution rates. A dynamic equilibrium between catalyst bulk, surface, and double layer is required for durability. In Concept 2, we establish that the effects of oxygen vacancies on a material's electronic properties and surface reconstruction are facet dependent. Combining doping and selective vacancy strategies is promising for activating CoOOH/NiOOH OER active surfaces. In

Concept 3, we show that the precise introduction of oxygen vacancies can selectively change the dominant reaction coordinate of the OER between the AEM and the more active LOM. In Concept 4, we summarize and examine recent *operando* works on possible surface reconstruction pathways in Co-based OER catalysts. Oxygen vacancy-mediated adsorption of  $OH^-$  and  $H_2O$  at low applied potentials is key for a highly active reconstructed CoOOH surface. However, high oxygen vacancy densities can initiate chemical or electrochemical active site quenching. In Concept 5, we highlight a remarkably common oxygen vacancy quantification XPS error (531 eV O 1s) and critically examine more accurate quantification techniques.

There is mounting evidence that oxygen vacancies, formed both *via* precatalyst modification methods and *in situ* metal dissolution, can determine the dominant surface reconstruction pathway and ultimate electrocatalyst activity. Fully understanding and influencing the surface reconstruction pathway of OER catalysts promises to increase the reconstructed active site density and activity. By continuing to combine *operando* surface characterization with rigorous oxygen vacancy quantification techniques, we expect that the vacancy thresholds for selectively steering the reaction mechanism and reconstruction pathway will be understood in the near future. Future work should focus on systematically introducing—and thoroughly quantifying—selected oxygen vacancy densities in a range of materials to observe trends in the mechanism steering thresholds. Selectively activating the LOER will enable escape from the universal scaling relationships limiting the activity of catalysts following the AEM.

## Author contributions

KC: conceptualization, investigation, visualization, writing – original draft; TJS: supervision, writing – review & editing; EF: conceptualization, funding acquisition, project administration, supervision, writing – review & editing.

## Conflicts of interest

There are no conflicts to declare.





## Data availability

No primary research results, software or code have been included and no new data were generated or analyzed as part of this review.

## Acknowledgements

KC and EF gratefully acknowledge the Swiss National Science Foundation through its PRIMA grant (grant no. PR00P2\_193111). KC thanks Mikhail Agrachev, Albert Schuler, and Ekaterina Pomjakushina for clarifying discussions about EPR, TGA-ICP-OES, and iodometric titration respectively.

## References

- 1 I. C. Man, H. Su, F. Calle-Vallejo, H. A. Hansen, J. I. Martínez, N. G. Inoglu, J. Kitchin, T. F. Jaramillo, J. K. Nørskov and J. Rossmeisl, *ChemCatChem*, 2011, **3**, 1159–1165.
- 2 J. O. Bockris and T. Otagawa, *J. Phys. Chem.*, 1983, **87**, 2960–2971.
- 3 J. S. Yoo, X. Rong, Y. Liu and A. M. Kolpak, *ACS Catal.*, 2018, **8**, 4628–4636.
- 4 A. Grimaud, O. Diaz-Morales, B. Han, W. T. Hong, Y.-L. Lee, L. Giordano, K. A. Stoerzinger, M. T. M. Koper and Y. Shao-Horn, *Nat. Chem.*, 2017, **9**, 457–465.
- 5 T. Binninger, R. Mohamed, K. Waltar, E. Fabbri, P. Levecque, R. Koetz and T. J. Schmidt, *Sci. Rep.*, 2015, **5**, 12167.
- 6 X. Rong, J. Parolin and A. M. Kolpak, *ACS Catal.*, 2016, **6**, 1153–1158.
- 7 E. Fabbri, M. Nachttegaal, T. Binninger, X. Cheng, B.-J. Kim, J. Durst, F. Bozza, T. Graule, R. Schaublin, L. Wiles, M. Pertoso, N. Danilovic, K. E. Ayers and T. J. Schmidt, *Nat. Mater.*, 2017, **16**, 925.
- 8 A. E. Thorarinsdottir, S. S. Veroneau and D. G. Nocera, *Nat. Commun.*, 2022, **13**, 12433.
- 9 W. Liu, J. Yu, T. Li, S. Li, B. Ding, X. Guo, A. Cao, Q. Sha, D. Zhou, Y. Kuang and X. Sun, *Nat. Commun.*, 2024, **15**, 4712.
- 10 D. Zhou, F. Li, Y. Zhao, L. Wang, H. Zou, Y. Shan, J. Fu, Y. Ding, L. Duan, M. Liu, L. Sun and K. Fan, *ACS Catal.*, 2023, **13**, 4398–4408.
- 11 J. Ferreira de Araujo, F. Dionigi, T. Merzdorf, H. S. Oh and P. Strasser, *Angew. Chem., Int. Ed.*, 2021, **60**, 14981–14988.
- 12 Z.-F. Huang, J. Song, Y. Du, S. Xi, S. Dou, J. M. V. Nsanzimana, C. Wang, Z. J. Xu and X.-S. Wang, *Nat. Energy*, 2019, **4**, 329–338.
- 13 A. Moysiadou, S. Lee, C.-S. Hsu, H. M. Chen and X. Hu, *J. Am. Chem. Soc.*, 2020, **142**, 11901–11914.
- 14 C. Rong, X. Huang, H. Arandiyana, Z. Shao, Y. Wang and Y. Chen, *Adv. Mater.*, 2025, **37**, 2416362.
- 15 L. G. Li, Q. Shao and X. Q. Huang, *Chem. – Eur. J.*, 2020, **26**, 3943–3960.
- 16 S. Anantharaj and S. Noda, *Small*, 2020, **16**, 24.
- 17 T. M. Pham, M. Plevova, S. Bartling, N. Rockstroh, A. Springer, A. Slabon, J. Hnat, A.-E. Surkus and R. Francke, *J. Catal.*, 2024, **438**, 115675.
- 18 H. B. Tao, L. Fang, J. Chen, H. B. Yang, J. Gao, J. Miao, S. Chen and B. Liu, *J. Am. Chem. Soc.*, 2016, **138**, 9978–9985.
- 19 M. Lu, Y. Zheng, Y. Hu, B. Huang, D. Ji, M. Sun, J. Li, Y. Peng, R. Si, P. Xi and C.-H. Yan, *Sci. Adv.*, 2022, **8**, eabq3563.
- 20 X. Miao, L. Wu, Y. Lin, X. Yuan, J. Zhao, W. Yan, S. Zhou and L. Shi, *Chem. Commun.*, 2019, **55**, 1442–1445.
- 21 X. Cheng, E. Fabbri, Y. Yamashita, I. E. Castelli, B. Kim, M. Uchida, R. Haumont, I. Puente-Orench and T. J. Schmidt, *ACS Catal.*, 2018, **8**, 9567–9578.
- 22 F. Song, K. Schenk and X. Hu, *Energy Environ. Sci.*, 2016, **9**, 473–477.
- 23 H. Xiao, H. Yin, X. Li, X. Zhou, W. Zhang, F. Pan, J. Zhao, J. Guo, S. Li and L. Qian, *Sustainable Mater. Technol.*, 2024, **40**, e00955.
- 24 J. Liu, J. Nai, T. You, P. An, J. Zhang, G. Ma, X. Niu, C. Liang, S. Yang and L. Guo, *Small*, 2018, **14**, 1703514.
- 25 Z. Xiao, Y.-C. Huang, C.-L. Dong, C. Xie, Z. Liu, S. Du, W. Chen, D. Yan, L. Tao, Z. Shu, G. Zhang, H. Duan, Y. Wang, Y. Zou, R. Chen and S. Wang, *J. Am. Chem. Soc.*, 2020, **142**, 12087–12095.
- 26 D. Chen, M. Qiao, Y.-R. Lu, L. Hao, D. Liu, C.-L. Dong, Y. Li and S. Wang, *Angew. Chem., Int. Ed.*, 2018, **57**, 8691–8696.
- 27 R. Zhang, Y.-C. Zhang, L. Pan, G.-Q. Shen, N. Mahmood, Y.-H. Ma, Y. Shi, W. Jia, L. Wang, X. Zhang, W. Xu and J.-J. Zou, *ACS Catal.*, 2018, **8**, 3803–3811.
- 28 R. Zhang, L. Pan, B. Guo, Z.-F. Huang, Z. Chen, L. Wang, X. Zhang, Z. Guo, W. Xu, K. P. Loh and J.-J. Zou, *J. Am. Chem. Soc.*, 2023, 2271–2281.
- 29 A. Moysiadou and X. Hu, *J. Mater. Chem. A*, 2019, **7**, 25865–25877.
- 30 C. Qiu, F. Maroun, M. Bouvier, I. Pacheco, P. Allongue, T. Wiegmann, C. Hendric Scharf, V. de Manuel-Gonzalez, F. Reikowski, J. Stettner and O. M. Magnussen, *ChemCatChem*, 2024, **16**, e202400988.
- 31 E. M. Davis, A. Bergmann, C. Zhan, H. Kühlenbeck and B. R. Cuenya, *Nat. Commun.*, 2023, **14**, 4791.
- 32 P. P. Lopes, D. Y. Chung, X. Rui, H. Zheng, H. He, P. Farinazzo Bergamo Dias Martins, D. Strmcnik, V. R. Stamenkovic, P. Zapol, J. F. Mitchell, R. F. Klie and N. M. Markovic, *J. Am. Chem. Soc.*, 2021, **143**, 2741–2750.
- 33 H. He, T. Matsuda, A. Miura, M. Nagao, J. K. Padarti, T. Ohno and S. Hirai, *Sustainable Energy Fuels*, 2024, **8**, 789–796.
- 34 B. He, P. Hosseini, D. Escalera-López, J. Schulwitz, O. Rüdiger, U. Hagemann, M. Heidelmann, S. DeBeer, M. Muhler, S. Cherevko, K. Tschulik and T. Li, *Adv. Energy Mater.*, 2025, **15**, 2403096.
- 35 P. W. Menezes, A. Indra, A. Bergmann, P. Cherev, C. Walter, H. Dau, P. Strasser and M. Driess, *J. Mater. Chem. A*, 2016, **4**, 10014–10022.
- 36 Y. Sato, Y. Aoki, K. Takase, H. Kiuchi, D. Kowalski and H. Habazaki, *ACS Appl. Energy Mater.*, 2020, **3**, 5269–5276.
- 37 Y. Wei, Y. Hu, P. Da, Z. Weng, P. Xi and C.-H. Yan, *Proc. Natl. Acad. Sci. U. S. A.*, 2023, **120**, e2312224120.
- 38 X. Chen, X. Xu, C. Shao, Z. Ke, Y. Cheng, H. Jin, Y. Da, D. Liu and W. Chen, *ACS Energy Lett.*, 2024, **9**, 2182–2192.
- 39 E. M. Davis, A. Bergmann, H. Kühlenbeck and B. Roldan Cuenya, *J. Am. Chem. Soc.*, 2024, **146**, 13770–13782.
- 40 Y. Wei, Z. Zhang, C. Mei, J. Tan, Z. Wang, J. Li and L. Gan, *Chem. Mater.*, 2023, **35**, 4461–4470.
- 41 K. Shojaei, A. Montoya and B. S. Haynes, *Comput. Mater. Sci.*, 2013, **72**, 15–25.
- 42 H. Zhu, X. Song, X. Han, X. Zhang, J. Bao, N. Zhang and G. He, *Environ. Sci. Technol.*, 2020, **54**, 8601–8611.
- 43 J. T. Mefford, A. R. Akbashev, M. Kang, C. L. Bentley, W. E. Gent, H. D. Deng, D. H. Alsem, Y.-S. Yu, N. J. Salmon, D. A. Shapiro, P. R. Unwin and W. C. Chueh, *Nature*, 2021, **593**, 67–73.
- 44 S. Wang, Q. Jiang, S. Ju, C.-S. Hsu, H. M. Chen, D. Zhang and F. Song, *Nat. Commun.*, 2022, **13**, 6650.
- 45 Y. Yao, G. Zhao, X. Guo, P. Xiong, Z. Xu, L. Zhang, C. Chen, C. Xu, T.-S. Wu, Y.-L. Soo, Z. Cui, M. M.-J. Li and Y. Zhu, *J. Am. Chem. Soc.*, 2024, **146**, 15219–15229.
- 46 S. Haschke, M. Mader, S. Schlicht, A. M. Roberts, A. M. Angeles-Boza, J. A. C. Barth and J. Bachmann, *Nat. Commun.*, 2018, **9**, 4565.
- 47 H. Han and H. Frei, *J. Phys. Chem. C*, 2008, **112**, 16156–16159.
- 48 M. Zhang, M. de Respinis and H. Frei, *Nat. Chem.*, 2014, **6**, 362–367.
- 49 J. F. de Araujo, F. Dionigi, T. Merzdorf, H.-S. Oh and P. Strasser, *Angew. Chem., Int. Ed.*, 2021, **60**, 14981–14988.
- 50 S. Lee, K. Banjac, M. Lingensfelder and X. Hu, *Angew. Chem., Int. Ed.*, 2019, **58**, 10295–10299.
- 51 A. Bergmann, T. E. Jones, E. Martinez Moreno, D. Teschner, P. Cherev, M. Gliech, T. Reier, H. Dau and P. Strasser, *Nat. Catal.*, 2018, **1**, 711–719.
- 52 C. Alex, S. C. Sarma, S. C. Peter and N. S. John, *ACS Appl. Energy Mater.*, 2020, **3**, 5439–5447.
- 53 J. N. Hausmann, S. Mebs, H. Dau, M. Driess and P. W. Menezes, *Adv. Mater.*, 2022, **34**, 2207494.
- 54 C. L. Farrow, D. K. Bediako, Y. Surendranath, D. G. Nocera and S. J. L. Billinge, *J. Am. Chem. Soc.*, 2013, **135**, 6403–6406.
- 55 G. Kwon, H. Jang, J.-S. Lee, A. Mane, D. J. Mandia, S. R. Soltau, L. M. Utschig, A. B. F. Martinson, D. M. Tiede, H. Kim and J. Kim, *J. Am. Chem. Soc.*, 2018, **140**, 10710–10720.
- 56 G. Chen, Z. W. Hu, Y. P. Zhu, B. B. Gu, Y. J. Zhong, H. J. Lin, C. T. Chen, W. Zhou and Z. P. Shao, *Adv. Mater.*, 2018, **30**, 8.
- 57 X. Ma, W. Zhang, Y. Deng, C. Zhong, W. Hu and X. Han, *Nanoscale*, 2018, **10**, 4816–4824.
- 58 Y. Pan, H. Ren, H. Du, F. Cao, Y. Jiang, H. Du and D. Chu, *J. Mater. Chem. A*, 2018, **6**, 22497–22502.
- 59 X. Leng, K.-H. Wu, Q. Zeng, I. R. Gentle and D.-W. Wang, *Asia-Pac. J. Chem. Eng.*, 2016, **11**, 415–423.





- 60 R. Sanchis-Gual, D. Hunt, C. Jaramillo-Hernández, A. Seijas-Da Silva, M. Mizrahi, C. Marini, V. Oestreicher and G. Abellán, *ACS Catal.*, 2023, **13**, 10351–10363.
- 61 F. Dionigi, Z. Zeng, I. Sinev, T. Merzdorf, S. Deshpande, M. B. Lopez, S. Kunze, I. Zegkinoglou, H. Sarodnik, D. Fan, A. Bergmann, J. Drnec, J. F. Araujo, M. Gliech, D. Teschner, J. Zhu, W. X. Li, J. Greeley, B. R. Cuenya and P. Strasser, *Nat. Commun.*, 2020, **11**, 2522.
- 62 M. Wang, Z. Wang, Y. Zhang, Y. Shi, T.-S. Chan, S.-C. Haw, J. Wang, H. Wang, S. Wang, H. Fei, R. Liu, T. Liu, C.-F. Yan and J. Wang, *ACS Energy Lett.*, 2024, **9**, 5502–5508.
- 63 K. Fan, D. Zhou, H. Yang, L. Wang, Y. Shan, M. Wan, A. Zheng and L. Sun, *ACS Catal.*, 2025, 3256–3266.
- 64 X. Liu and C. T. Prewitt, *Phys. Chem. Miner.*, 1990, **17**, 168–172.
- 65 Q. Zhao and H. J. Kulik, *J. Chem. Theory Comput.*, 2018, **14**, 670–683.
- 66 M. Deliens and H. Goethals, *Mineral. Mag.*, 1973, **39**, 152–157.
- 67 H. Idriss, *Surf. Sci.*, 2021, **712**, 121894.
- 68 J. Wang, D. N. Mueller and E. J. Crumlin, *J. Eur. Ceram. Soc.*, 2024, **44**, 116709.
- 69 S. Yamamoto, H. Bluhm, K. Andersson, G. Ketteler, H. Ogasawara, M. Salmeron and A. Nilsson, *J. Phys.: Condens. Matter*, 2008, **20**, 184025.
- 70 A. Boucly, L. Artiglia, E. Fabbri, D. Palagin, D. Aegerter, D. Pergolesi, Z. Novotny, N. Comini, J. T. Diulus, T. Huthwelker, M. Ammann and T. J. Schmidt, *J. Mater. Chem. A*, 2022, **10**, 2434–2444.
- 71 B. V. Crist, The International XPS Database: Oxygen (O), 2025, <https://xpsdatabase.net/oxygen-o-z8/>.
- 72 M. Li, L. Zhang, W. Liu, Y. Jin and B. Li, *Talanta*, 2025, **282**, 126969.
- 73 M. Li, L. Zhang, W. Liu, Y. Jin and B. Li, *Anal. Chem.*, 2024, **96**, 8999–9006.
- 74 E. Giamello, M. Chiesa and M. C. Paganini, in *Point Defects in Electron Paramagnetic Resonance*, ed. J. Jupille and G. Thornton, Springer International Publishing, Cham, 2015, pp. 303–326.
- 75 K. Dyrek and M. Che, *Chem. Rev.*, 1997, **97**, 305–332.
- 76 R.-A. Eichel, *Phys. Chem. Chem. Phys.*, 2011, **13**, 368–384.
- 77 T. Pinheiro Araújo, C. Mondelli, M. Agrachev, T. Zou, P. O. Willi, K. M. Engel, R. N. Grass, W. J. Stark, O. V. Safonova, G. Jeschke, S. Mitchell and J. Pérez-Ramírez, *Nat. Commun.*, 2022, **13**, 5610.
- 78 E. Marelli, J. Gazquez, E. Poghosyan, E. Mueller, D. J. Gawryluk, E. Pomjakushina, D. Sheptyakov, C. Piamonteze, D. Aegerter, T. J. Schmidt, M. Medarde and E. Fabbri, *Angew. Chem., Int. Ed.*, 2021, **60**, 14609–14619.
- 79 K. Conder, E. Pomjakushina, A. Soldatov and E. Mitberg, *Mater. Res. Bull.*, 2005, **40**, 257–263.
- 80 W. M. Chen, W. Hong, J. F. Geng, X. S. Wu, W. Ji, L. Y. Li, L. Qui and X. Jin, *Phys. C*, 1996, **270**, 349–353.

